Ceramics International 51 (2025) 9579–9587

Contents lists available at ScienceDirect

Ceramics International

journal homepage: www.elsevier.com/locate/ceramint

# Effect of carbon vacancy on phase formation and mechanical properties of high-entropy (Ti,Nb,Ta,Hf,W)$C_x$

Wei Liao [a], Zhen Teng [b,**], Yiwang Bao [b,*]

[a] Department of Materials Science and Engineering, University of Science and Technology of China, CAS Key Laboratory of Materials for Energy Conversion, Hefei, Anhui, 230026, China

[b] Henan Key Laboratory of High-Performance Carbon Fiber Reinforced Composites, Institute of Carbon Matrix Composites, Henan Academy of Sciences, Zhengzhou, 450046, China

ARTICLE INFO

Handling Editor: P. Vincenzini

*Keywords:*
High-entropy
Carbides
Non-stoichiometry
Spark plasma sintering
Mechanical properties

ABSTRACT

High-entropy $(Ti_{0.2}Nb_{0.2}Ta_{0.2}Hf_{0.2}W_{0.2})C_x$ with different carbon vacancies were prepared from raw binary carbides in this study. The influences of stoichiometry, particle size of raw powder, and sintering temperature on phase formation, microstructure, and mechanical properties of $(Ti_{0.2}Nb_{0.2}Ta_{0.2}Hf_{0.2}W_{0.2})C_x$ were systematically investigated. The results indicate that the introduction of carbon vacancies and using finer raw binary carbide powders can both significantly enhance the formation ability of single-phase composition with uniform elemental distributions. The formation of a high-entropy phase could enhance the Vicker's hardness. The flexural strength is greatly influenced by the content of carbon vacancy, which is greatly detrimental to flexural strength. The fracture toughness is determined by both the content of carbon vacancies and the presence of secondary phases. By optimizing the content of carbon vacancies, particle size of raw powders, and sintering temperature, $(Ti_{0.2}Nb_{0.2}Ta_{0.2}Hf_{0.2}W_{0.2})C$ shows super high flexural strength of 743 MPa and fracture toughness of 8.6 MPa $m^{-1/2}$.

## 1. Introduction

High-entropy transition metal carbides (TMCs) comprising five components randomly occupying the metal sublattice exhibit many interesting physical and mechanical properties, such as higher hardness, higher room-temperature and high-temperature mechanical strength, improved corrosion resistance and irradiation resistance, lower thermal conductivity, and et al. [1–5]. Therefore, high-entropy TMCs have many promising applications in cutting tools, future hypersonic vehicles, and high-temperature nuclear reactors [6–12]. Much effort has been devoted to the prediction, design, and synthesis of new single-phase high--entropy TMCs [13–19].

Kenneth S. Vecchio et al. have proposed an entropy forming ability (EFA) descriptor to evaluate the synthesizability of single-phase five-metal high-entropy TMCs [8]. According to their calculations, most W-containing compositions exhibit relatively lower EFA around the critical value of EFA = 50 eV/atom$^{-1}$ above which a single-phase solid solution can be formed [8,13]. There exists one exception of the (VNbTaMoW)C which exhibits a high EFA = 130 eV/atom$^{-1}$. Therefore, several studies have reported the synthesis and properties of (VNbTaMoW)C and (VNbTaMoW)$C_x$ [7,20–22]. However, the reports of other W-containing high-entropy carbides with dense and uniform elemental distributions are still rare, especially for those synthesized directly from binary precursor carbides [23]. X. Wei et al. prepared (TiHfNbTaW)C from five transition metal oxides and graphite, and discovered gradient distributions of the residual graphite content and hardness [24]. The same group fabricated high-entropy (TiZrNbTaW)C from different starting materials, and discovered that using binary carbides as raw materials resulted in homogeneous elemental distribution but with relatively lower relative density [25]. J. Potschke et al. [26] and Y. Zhu et al. [27] both reported the successful fabrication of single-phase (TaNbTiVW)C high-entropy carbides from binary carbides.

The introduction of carbon vacancies seems a novel routine to promote the solid solution in high-entropy compositions due to the enhanced mass diffusion [28–30]. Correspondingly, the mechanical and thermophysical properties can be tuned by the introduction of carbon vacancies [12,21,28,31]. D. Liu et al. systematically studied the phase, mechanical and thermal properties of (VNbTaMoW)Cx with different

* Corresponding author.
** Corresponding author.
*E-mail addresses:* tengzhen426@163.com (Z. Teng), ywbao@ctc.ac.cn (Y. Bao).

https://doi.org/10.1016/j.ceramint.2024.10.429
Received 20 August 2024; Received in revised form 14 October 2024; Accepted 29 October 2024
Available online 29 October 2024

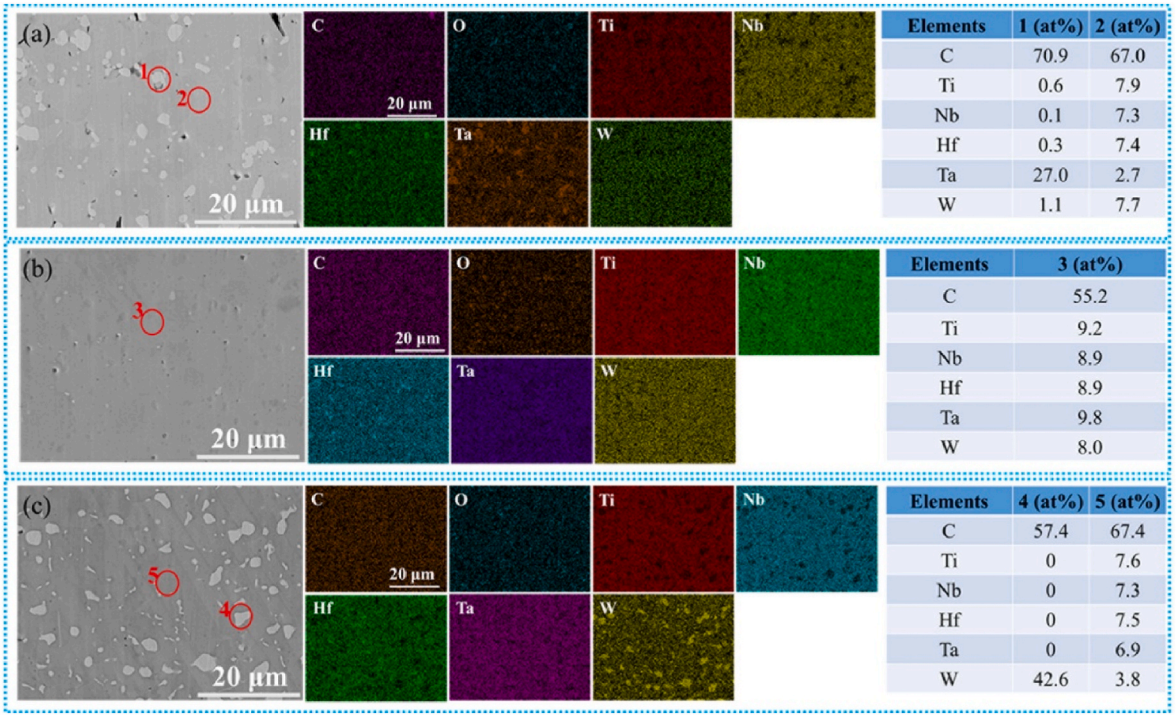


| Elements | 1 (at%) | 2 (at%) |
|---|---|---|
| C | 70.9 | 67.0 |
| Ti | 0.6 | 7.9 |
| Nb | 0.1 | 7.3 |
| Hf | 0.3 | 7.4 |
| Ta | 27.0 | 2.7 |
| W | 1.1 | 7.7 |

| Elements | 3 (at%) |
|---|---|
| C | 55.2 |
| Ti | 9.2 |
| Nb | 8.9 |
| Hf | 8.9 |
| Ta | 9.8 |
| W | 8.0 |

| Elements | 4 (at%) | 5 (at%) |
|---|---|---|
| C | 57.4 | 67.4 |
| Ti | 0 | 7.6 |
| Nb | 0 | 7.3 |
| Hf | 0 | 7.5 |
| Ta | 0 | 6.9 |
| W | 42.6 | 3.8 |

**Fig. 1.** Surface microstructure and corresponding EDS mapping with element composition of polishing cross-section of (a) C1.0-2200; (b) C0.9-2200; (c) C0.8-2200.

carbon stoichiometry, and discovered that a highly carbon-deficient condition will give rise to structure disintegration, and the nanohardness and flexure strength exhibit peak values at x = 0.8 [21]. However, the influences of carbon stoichiometry on the phase formation and mechanical properties of those W-containing high-entropy carbides with lower EFA values are still unclear. Through the introduction of carbon vacancies, it is promising to obtain more W-containing high-entropy carbides with lower EFA values and achieve higher mechanical properties.

Besides, the particle sizes of the constituent binary carbide raw materials are also important factors in the fabrication of single-phase high-entropy carbides [4,32]. Fine particle size could promote the mutual solid solution of different carbides and will be helpful for the formation of uniform high-entropy carbides. Therefore, it is also of great interest to investigate the particle size of the raw materials on the phase formation of high-entropy carbides.

Considering TaC, WC binary carbides have excellent thermal-mechanical properties [33,34].In this study, $(Ti_{0.2}Nb_{0.2}Ta_{0.2}Hf_{0.2}W_{0.2})C_x$ with different carbon stoichiometry were prepared from binary precursor carbides with different particle sizes and $TiH_2$ by spark plasma sintering (SPS), where the carbon stoichiometry (x) is 0.8, 0.9 and 1.0. The influences of carbon content and raw material particle size on the phase formation and mechanical were systematically investigated.

## 2. Experimental

$(Ti_{0.2}Nb_{0.2}Ta_{0.2}Hf_{0.2}W_{0.2})C_x$ was prepared using TiC (Aladdin, 99 % purity, 2–4 μm powder size), NbC (Aladdin, 99 % purity, 1–4 μm powder size), coarse TaC (Aladdin, 99.5 % purity, ≤3 μm powder size), fine TaC (Changyu, 99.5 % purity, ≤500 nm powder size), HfC (Aladdin, 99.5 % purity, 2–4 μm powder size), WC (Aladdin, 99 % purity, ≤1 μm powder size) and $TiH_2$ (Forsman, 99.5 % purity, ≤45 μm powder size) as raw materials. The raw powders were mixed according to the designed formulas $(Ti_{0.2}Nb_{0.2}Ta_{0.2}Hf_{0.2}W_{0.2})C_x$ (x = 1.0, 0.9, 0.8) considering the reactions shown in equation (1).

$$5xTiH_2 + (1-5x)TiC + NbC + TaC + HfC + WC = 5\left(Ti_{0.2}Nb_{0.2}Ta_{0.2}Hf_{0.2}W_{0.2}\right)C_{1-x} + 5xH_2\uparrow \quad (1)$$

The slurries were ball milled for 5 h using ethanol as milling media. Then they were dried in vacuum, sieved, and sintered by spark plasma sintering (SPS). The sintering temperatures were chosen to be 2200 °C,2100 °C, and 2000 °C respectively. The dwell time is 5 min and a uniaxial pressure of 50 MPa was applied.

Densities ($\rho$) were measured by the Archimedes' method. The microstructures and element distribution were observed using scanning electron microscopy (SEM, Zeiss) equipped with Energy Dispersive X-ray Spectroscopy (EDS). The volume fraction of the second phase is measured by using the ImageJ software to estimate the relative area of the second phase in the SEM image. And the actual elemental content of the sample was determined by Electron Probe Micro Analysis (EPMA). X-ray diffraction (XRD) patterns were collected using a Panalytical X'Pert diffractometer with the Cu Kα radiation (XRD, Bruker AXS Ltd.) to identify the phase composition of $(Ti_{0.2}Nb_{0.2}Ta_{0.2}Hf_{0.2}W_{0.2})C_x$. In addition, the phase composition and microstructure of $(Ti_{0.2}Nb_{0.2}Ta_{0.2}Hf_{0.2}W_{0.2})C_x$ were further identified and verified by TEM (TEM, JMF-2100 F) characterization.

The Vickers hardness was determined by the Vickers diamond indentation method using an indentation load of 9.8 N with a 15 s dwell time. The flexural strength was measured using a three-point bending method on a rectangular bar with a size of 3 mm × 4 mm × 36 mm. A span size of 30 mm and a crosshead speed of 0.5 mm/min were applied. The fracture toughness was tested by a single-edge notched beam method (SENB), using a polished rectangular bar with a size of 2 mm ×

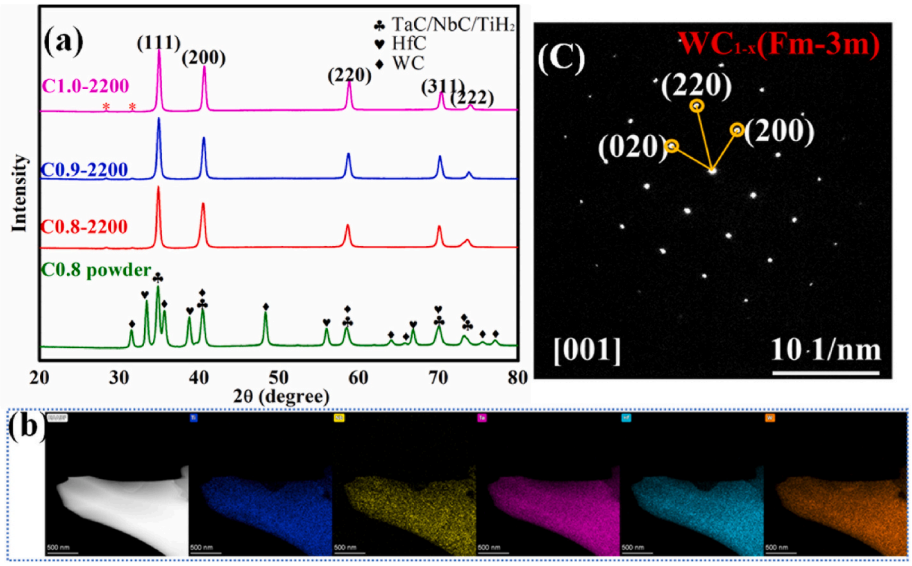


**Fig. 2.** (a)XRD characterization of C1.0–2200, C0.9–2200, C0.8-2200, and C0.8 mixed powder (b) the EDS spectrum of C0.8-2200 (c) SAED diagram of the [100] axis of the second phase of C0.8-2200.

4 mm × 38 mm and a notch of 2 mm depth. The span size of the test was 30 mm and the crosshead speed was 0.05 mm/min. The grain size was measured by polished SEM images after acid etching. Where the polished sample was completely immersed in acid solution for around 5 min, and then ultrasonic cleaning with ethanol as the medium for 10 min to obtain the corroded cross-section of the sample.

## 3. Results and discussions

### 3.1. Influence of carbon vacancy

Fig. 1 shows the SEM and EDS mapping of polished cross sections of $(Ti_{0.2}Nb_{0.2}Ta_{0.2}Hf_{0.2}W_{0.2})C_x$ prepared from coarse raw powders and sintered at 2200 °C. They were termed as C1.0–2200, C0.9–2200C0.8-2200 respectively. All three specimens show dense microstructure. For C1.0-2200 without carbon vacancies, a distinct secondary phase can be observed. According to the EDS analysis, the secondary phase can be determined to be TaC. The main phase is a uniform solid solution of (Ti, Nb, Ta, Hf, W)C with a lower Ta content. The volume fraction of the second phase TaC was calculated to be 8.9 vol%. With the introduction of 10 % carbon vacancies, a single-phase high-entropy $(Ti_{0.2}Nb_{0.2}Ta_{0.2}Hf_{0.2}W_{0.2})C_{0.9}$ was obtained. Besides, minor oxides' secondary phases can be observed. EDS mapping shows homogeneous metal element distributions, which indicates the fully solid solution of various carbides and the formation of a high-entropy phase. However, with further increasing the content of carbon vacancies to 20 %, a new secondary phase begins to appear. The new secondary phase corresponds to tungsten carbide according to the EDS analysis, while the main phase shows less W content compared with Ti, Nb, Ta, and Hf. It indicates that when the carbon vacancy content is higher than a certain critical value, the second phase containing W gradually tends to appear, which is similar to the phase decomposition of $(VNbTaMoW)_{0.5}C_x$ and $(ZrHfVNbMoW)C_x$ [21,35]. The volume fraction of tungsten carbide was calculated to be around 7.1 vol%.

The XRD patterns of three high-entropy carbides along with the mixed raw powders of C0.8-2200 are shown in Fig. 2(a). Interestingly all three high-entropy carbides with different carbon vacancies show single-phases with a rock salt crystal structure. Although both C1.0–2200 and C0.8-2200 exhibit obvious second phases, the XRD patterns in Fig. 2(a) do not display peak splitting or additional characteristic peaks. The lattice parameter of TaC is 4.455 Å, which is similar to the lattice parameter of 4.445 Å of the C1.0-2200 carbides obtained by XRD fitting. In the XRD diffraction of the experimental sample, the high-entropy carbides have weak diffraction peaks (*) representing $HfO_2$ between 2θ angles of 25°–30°.

Fig. 2(b) and (c) show the EDS spectrum of C0.8-2200 and the selected region electron diffraction (SAED) of the second phase [001] axis of C0.8-2200, respectively. Combined with the XRD and SEM characterization of C0.8-2200, the diffraction spots representing the FCC structure indicate that the second phase is $WC_{1-x}$ with an Fm-3m configuration crystal structure instead of WC with a hexagonal structure. The lattice constant of $WC_{1-x}$ is 4.456 Å, rather close to that of C0.8-2200(4.453 Å), demonstrating the crystallographic continuity of the two carbides [36]. Therefore, XRD patterns of all three samples show a single-phase structure. In addition, the EDS mapping of the three carbides prepared by the experiment showed a small amount of segregation of Hf and O elements, which was consistent with their XRD characterization in Fig. 2(a).

The emergence of the TaC second phase in C1.0-2200 bulks may be due to its higher activation energy and slower diffusion efficiency of Ta in cubic carbides [37,38]. The appearance of $WC_{1-x}$ in C0.8–2200 may be due to the increase of lattice distortion caused by the increase of

**Table 1**
Designed composition, sintering temperature, densities, average grain sizes, and mechanical property of C1.0–2200, C0.9-2200, and C0.8-2200.

| Sample | Designed composition | Sintering temperature (°C) | Density (g/cm$^3$) | Grain size (μm) | Vickers hardness (GPa) | Flexural strength (MPa) | Fracture toughness (MPa m$^{-1/2}$) |
|---|---|---|---|---|---|---|---|
| C1.0-2200 | (Ti,Nb,Ta,Hf,W)C | 2200 | 10.99 ± 0.007 | 6.2 | 20.9 ± 0.5 | 616 ± 5 | 7.1 ± 0.1 |
| C0.9-2200 | $(Ti,Nb,Ta,Hf,W)C_{0.9}$ | 2200 | 11.09 ± 0.109 | 10.6 | 22.2 ± 0.9 | 490 ± 16 | 5.5 ± 0.4 |
| C0.8-2200 | $(Ti,Nb,Ta,Hf,W)C_{0.8}$ | 2200 | 11.13 ± 0.052 | 5.6 | 19.6 ± 0.6 | 133 ± 8 | 6.8 ± 0.4 |

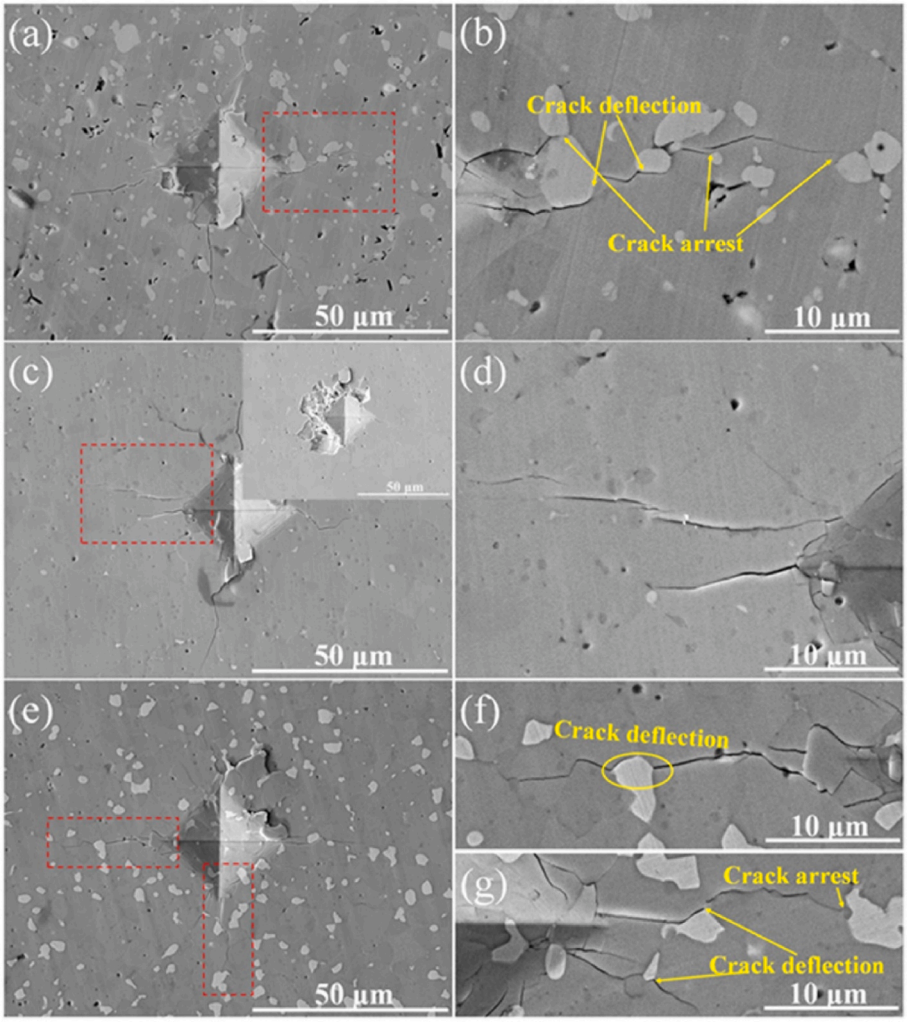


**Fig. 3.** The indentation morphology of (a)(b) C1.0-2100, (c)(d) C0.9-2100, and (e–g) C0.8-2100 and the enlarged view of corresponding radial crack.

carbon vacancy, and the low carbon vacancy tolerance of $WC_{1-x}$ makes it easier to precipitate at higher carbon vacancies [39].

The densities, average grain sizes, hardness, flexural strength, and fracture toughness of C1.0–2200, C0.9-2200, and C0.8-2200 are summarized in Table 1. The SEM image of three acid etched sample are shown in Fig. S1. The average grain sizes of C1.0–2200, C0.9-2200, and C0.8-2200 are 6.2 μm, 10.6 μm and 5.6 μm, respectively. Under the same sintering conditions, the grain size of C0.9-2200 is larger than those of C1.0–2200 and C0.8-2200. Normally, compositions with higher carbon vacancy content tend to show coarse grains due to enhanced atomic diffusions [10,12,40]. For C0.9-2200, the presence of carbon vacancies promotes mass diffusion and grain growth. While for C0.8-2200, it is reasonable that the $WC_{1-x}$ phase originates from the decomposition of $(Ti_{0.2}Nb_{0.2}Ta_{0.2}Hf_{0.2}W_{0.2})C_{0.8}$ phase during the cooling stage after sintering due to the similarity of the lattice structure of $WC_{1-x}$ and the main phase. Therefore, the decomposition of the main phase gave rise to the decrease in grain size.

The Vickers hardness of C0.9-2200 is 22.2 GPa, which is the highest among all three compositions. It agrees well with that single-phase high-entropy compositions tend to show higher hardness [41,42]. C1.0-2200 shows a Vickers hardness of 20.9 GPa, and C0.8-2200 shows the smallest Vickers hardness of 19.6 GPa. Carbon vacancy is more sensitive for the flexural strength of $(Ti_{0.2}Nb_{0.2}Ta_{0.2}Hf_{0.2}W_{0.2})C_x$. C1.0-2200 shows the highest flexural strength of 616 MPa, followed by 490 MPa for C0.9-2200 and 133 MPa for C0.8-2200. The flexural strength of $(Ti_{0.2}Nb_{0.2}Ta_{0.2}Hf_{0.2}W_{0.2})C_x$ decreases rapidly with the increase of carbon vacancy, which is well consistent with the literature [28].In terms of fracture toughness, C1.0-2200, and C0.8-2200 with secondary phases have similarly high fracture toughness values of 7.1 MPa $m^{-1/2}$ and 6.8 MPa $m^{-1/2}$, respectively, while the single-phase C0.9-2200 shows a relatively lower fracture toughness of $5.5 \pm 0.4$ MPa $m^{-1/2}$. This indicates that the introduction of secondary phases plays a decisive role in enhancing the toughness of high-entropy carbides. As shown in the Vickers indentation morphology of $(Ti_{0.2}Nb_{0.2}Ta_{0.2}Hf_{0.2}W_{0.2})C_x$ in Fig. 3, C0.9-2200 show straight and long cracks. C1.0–2200 and C0.8-2200 show clear crack deflections by the second phases and crack terminations at the second phases.

### 3.2. *Influence of particle size of raw powder*

Considering the secondary phase of TaC in C1.0-2200, the raw TaC powder was subsequently replaced by TaC (Changyu, 99.5 % purity, ≤500 nm powder size) with fine particle size. The sintering temperature was chosen to be 2100 °C due to fine particle size. The sintered samples were termed as C1.0-2100-F, C0.9-2100-F, and C0.8-2100-F, respectively, where F represents fine raw TaC powder.

Fig. 4 shows the SEM and EDS mapping of C1.0-2100-F, C0.9-2100-F, and C0.8-2100-F. The result demonstrates that fine TaC powder significantly promoted the solid solution of Ta. Both C1.0-2100-F and C0.9-2100-F form uniform solid solutions, as suggested by the homogenous metal element distributions. Similarly, C0.8-2100-F still shows segregation of W, as shown in Fig. 4(c). XRD patterns of the three carbides are

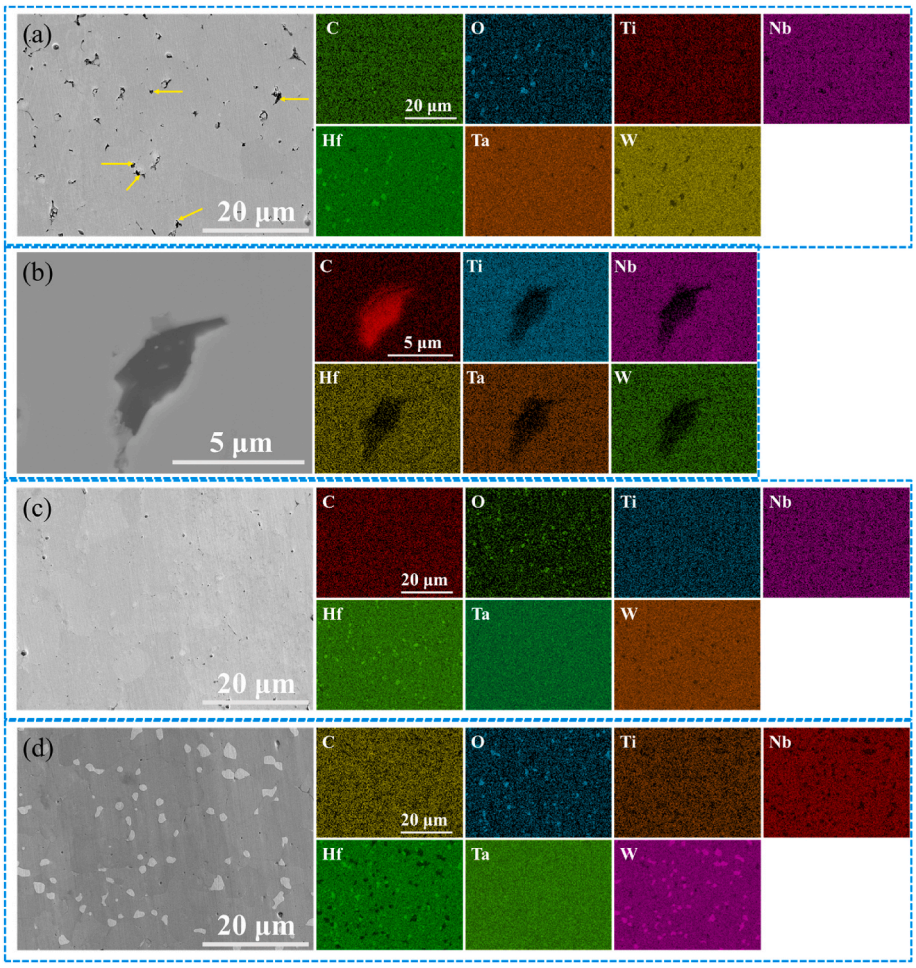


**Fig. 4.** Surface microstructure and corresponding EDS mapping of polishing cross-section of (a–b) C1.0-2100-F; (c) C0.9-2100-F; (d) C0.8-2100-F.

**Table 2**
Designed composition, sintering temperature, densities, average grain sizes, and mechanical property of C1.0-2100-F, C0.9-2100-F, and C0.8-2100-F.

| Sample | Designed composition | Sintering temperature (°C) | Density (g/cm$^3$) | Grain size (μm) | Vickers hardness (GPa) | Flexural strength (MPa) | Fracture toughness (MPa m$^{-1/2}$) |
|---|---|---|---|---|---|---|---|
| C1.0-2100-F | (Ti,Nb,Ta,Hf,W)C | 2100 | 10.92 ± 0.004 | 6.7 | 19.8 ± 0.7 | 646 ± 5 | 8.4 ± 0.2 |
| C0.9-2100-F | (Ti,Nb,Ta,Hf,W)$C_{0.9}$ | 2100 | 11.04 ± 0.001 | 6.8 | 20.9 ± 0.7 | 536 ± 9 | 5.2 ± 0.3 |
| C0.8-2100-F | (Ti,Nb,Ta,Hf,W)$C_{0.8}$ | 2100 | 11.14 ± 0.002 | 4.9 | 19.3 ± 0.6 | 177 ± 20 | 7.9 ± 0.2 |

shown in Fig. S2. All the XRD patterns are single rock salt structures, without the appearance of additional characteristic peaks or peak splitting. It can be inferred that C0.8-2100-F still has the $WC_{1-x}$ second phase with Fm-3m crystal structure. Minor oxides also appear in Fig. 4, which is consistent with the characteristic oxide peaks in the XRD patterns. The oxide secondary phases in C1.0-2100-F, C0.9-2100-F, and

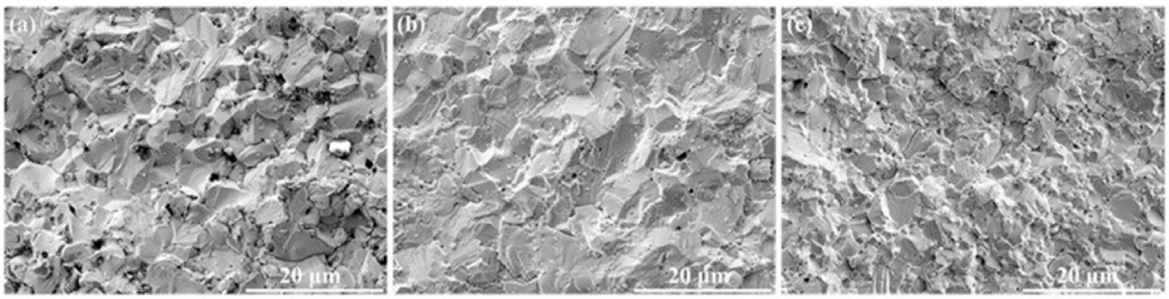


**Fig. 5.** SEM microstructure images of the fracture surface. (a) C1.0-2100-F; (b) C0.9-1200-F; (c) C0.8-2100-F.

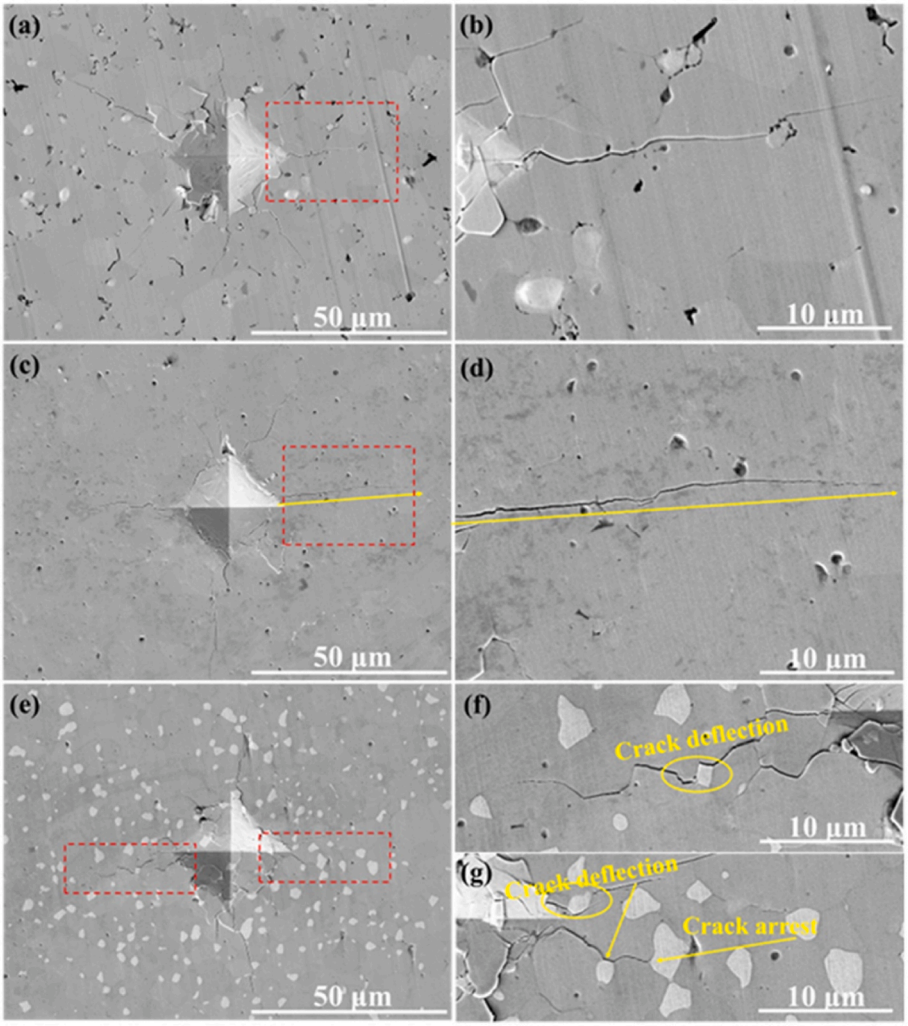


**Fig. 6.** The indentation morphology and enlarged view of corresponding radial crack. (a)(b) C1.0-2100-F; (c)(d) C0.9-2100-F; (e)(f) C0.8-2100-F.

C0.8-2100-F are more evident than their corresponding compositions with coarse TaC raw powder, generally because fine raw powders contain more oxidized surfaces. In addition, some residual carbon as indicated in Fig. 4(a) can be discovered in C1.0-2100-F, and this can be verified by the enlarged view and the corresponding EDS spectra shown in Fig. 4(b). The ratio of transition metal elements to C elements in Cx-2100-F samples was measured by EMPA. The results show that the proportions of C1.0-2100-F, C1.0-2100-F, C0.9-2100-F, and C0.8-2100-F are 1:1.02,1:0.91,1:0.82, respectively. With the increase of carbon vacancy, the residual carbon phase disappears. It suggests that the W-containing high-entropy carbides favor a certain amount of carbon vacancies, which is consistent with the Fm-3m structure of $WC_{1-x}$.

Table 2 shows the density, average grain size, and mechanical properties of C1.0-2100-F, C0.9-2100-F, and C0.8-2100-F. With the increase of carbon vacancy, the density of $(Ti_{0.2}Nb_{0.2}Ta_{0.2}Hf_{0.2}W_{0.2})C_x$ increases. The SEM images of polished surfaces and grain size statistical histograms of three acid-etched Cx-2100-F samples are shown in Fig. S3. The grain sizes for C1.0-2100-F, C0.9-2100-F, and C0.8-2100-F are 6.7 μm, 6.8 μm, and 4.9 μm respectively. C0.9-2100-F has the highest hardness value of 20.9 GPa, followed by 19.8 GPa of C1.0-2100-F and 19.3 GPa of C0.8-2100-F. The lower hardness of C1.0-2100-F than that of C0.9-2100-F can be ascribed to the presence of residual carbon. The hardness values of C1.0-2100-F, C0.9-2100-F, and C0.8-2100-F are relatively lower than their corresponding compositions prepared from coarse TaC powder, generally because of the increased oxides secondary phases. The difference in hardness between different samples becomes much weaker than that of those prepared from coarse TaC powder, which can be ascribed to the similar average grain sizes and similar phases.

The flexural strength decreases significantly with the increase of carbon vacancy. Similarly, this can be ascribed to the decreased atomic bonding with increasing carbon vacancy. The fracture surface morphologies of Cx-2100-F are shown in Fig. 5. For C1.0-2100-F, the fracture mode is intergranular dominant, suggesting the higher strength of single grain. C0.9-2100-F shows a mixture of transgranular and intergranular fracture modes, while C0.8-2100-F shows a transgranular dominant fracture mode implying the weaker strength of single grain due to weaker atomic bonding. C1.0-2100-F shows the highest mechanical strength of 646 MPa, which is slightly higher than that of C1.0-2200. The improvement of mechanical strength can be ascribed to the decrease of grain size and the elimination of the TaC secondary phase.

C1.0-2100-F and C0.8-2100-F exhibit high fracture toughness of 8.4 MPa $m^{-1/2}$ and 7.9 MPa $m^{-1/2}$, respectively. C0.9-2100-F has the lowest fracture toughness of 5.2 MPa $m^{-1/2}$. The indentation morphologies of Cx-2100-F are shown in Fig. 6. C0.9-2100-F exhibits straight and long cracks, which is similar to that of C0.9-2200 and is consistent with its lower fracture toughness. C1.0-2100-F exhibits crack deflections at grain boundaries, as shown in Fig. 6(a) and (b). Fig. 6(f) and (g) demonstrate the crack deflections both at grain boundaries and by those $WC_{1-x}$ grains. Besides, some cracks terminate at $WC_{1-x}$ grains. Both the

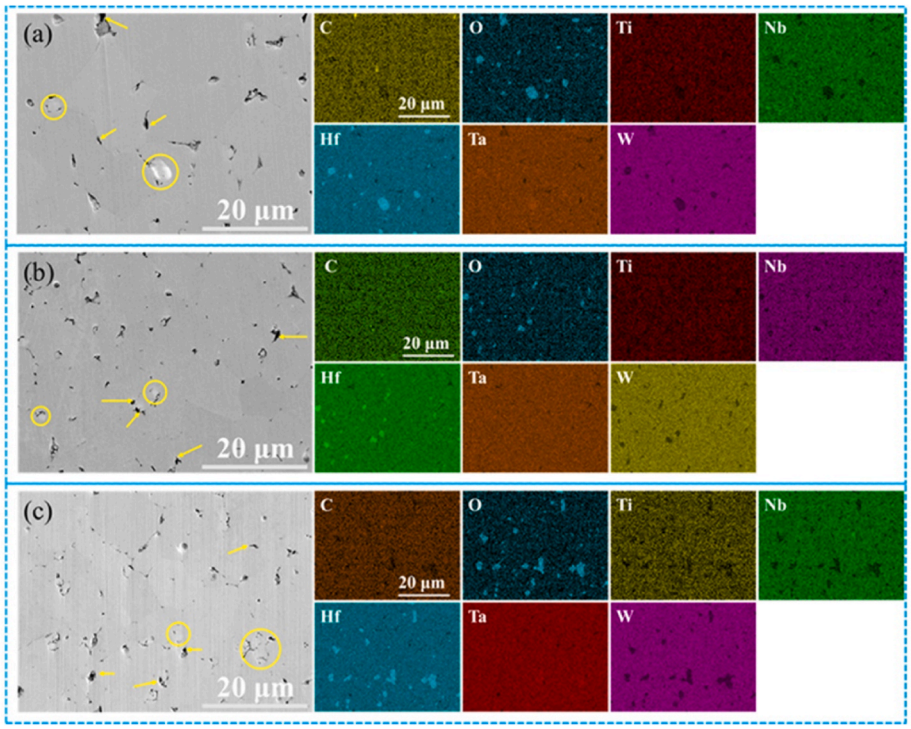


**Fig. 7.** Surface microstructure and corresponding EDS mapping of polishing cross-section of (a) C1.0-2200-F; (b) C1.0-2100-F; (c) C1.0-2000-F.

**Table 3**
Designed composition, sintering temperature, densities, average grain sizes, and mechanical property of C1.0-2200-F, C1.0-2100-F, and C1.0-2000-F.

| Sample | Designed composition | Sintering temperature (°C) | Density (g/cm$^3$) | Grain size (μm) | Vickers hardness (GPa) | Flexural strength (MPa) | Fracture toughness (MPa m$^{-1/2}$) |
|---|---|---|---|---|---|---|---|
| C1.0-2200-F | (Ti,Nb,Ta,Hf,W)C | 2200 | 10.87 ± 0.044 | 9.2 | 19.2 ± 0.7 | 516 ± 44 | 6.8 ± 0.3 |
| C1.0-2100-F | | 2100 | 10.92 ± 0.004 | 6.7 | 19.8 ± 0.7 | 646 ± 5 | 8.4 ± 0.2 |
| C1.0-2000-F | | 2000 | 10.94 ± 0.002 | 5.8 | 19.5 ± 0.5 | 743 ± 14 | 8.6 ± 0.4 |

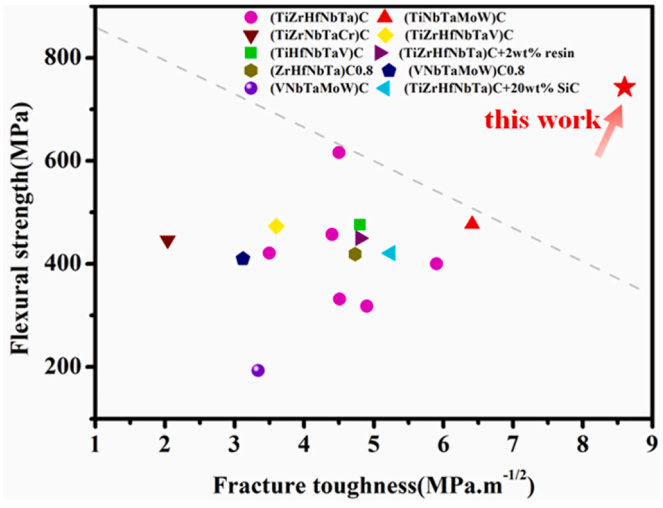


**Fig. 8.** The comparison of mechanical strength and fracture toughness among various high-entropy carbide compositions and the composition investigated in this study [20,30,40–47].

crack deflections and crack arrest give rise to a significant improvement in fracture toughness of C0.8-2100-F.

### 3.3. Influence of sintering temperature

The composition and mechanical properties of high-entropy ceramics are not only influenced by carbon vacancies but also significantly affected by sintering conditions [40,43]. Therefore, ($Ti_{0.2}Nb_{0.2}Ta_{0.2}Hf_{0.2}W_{0.2}$)C were sintered at different temperatures (2200 °C, 2100 °C, and 2000 °C) in order to optimize their mechanical properties. They were termed as C1.0-2200-F, C1.0-2100-F, and C1.0-2000-F, respectively. Fig. 7 shows the SEM and EDS mappings of the polished surfaces of those three specimens, which all show dense microstructures with homogeneous elemental distributions. Combined with XRD patterns in Fig. S4, it can be inferred that all three specimens are single-phase high-entropy carbides. It indicates that the presence of W promoted the formation of high-entropy phase as single-phase high-entropy ($Ti_{0.2}Nb_{0.2}Ta_{0.2}Hf_{0.2}W_{0.2}$)C can only be obtained when sintered as high as 2200 °C when prepared from binary carbides [43]. Besides, all three specimens show the presence of residue carbon (indicated by arrows) and oxides (indicated by circles).

Table 3 summarizes the density, grain size, and mechanical properties of C1.0-2200-F, C1.0-2100-F, and C1.0-2000-F. The SEM images of the etched surfaces and grain size statistical histograms of three samples are shown in Fig. S5. The average grain size decreases with the decrease

in sintering temperature, and C1.0-2000-F shows the smallest average grain size of 5.8 μm.

Both the flexural strength and fracture toughness increase monotonically with the decrease in sintering temperature. C1.0-2000-F shows the highest flexural strength of 743 MPa and the highest fracture toughness of 8.6 MPa $m^{-1/2}$. Fig. 8 shows the comparison of mechanical strength and fracture toughness among various high-entropy carbide compositions reported in the literature and the composition investigated in this study [21,32,44–51]. Most high-entropy exhibit flexural strength values between 300 MPa and 600 MPa, and fracture toughness values between 3 MPa $m^{-1/2}$ and 6 MPa $m^{-1/2}$. C1.0-2000-F in this study exhibits the highest flexural strength (743 MPa) and fracture toughness (8.6 MPa $m^{-1/2}$).

## 4. Conclusion

In this study, $(Ti_{0.2}Nb_{0.2}Ta_{0.2}Hf_{0.2}W_{0.2})C_x$ (x = 0.8, 0.9, and 1.0) were prepared by SPS from binary transition metal carbides with different particle sizes. Various high-entropy carbides with different phase compositions and microstructures were obtained. A certain degree of carbon vacancy and finer raw powders are favorable for the formation of single-phase high-entropy carbides. However, excessive carbon vacancies will lead to the segregation of $WC_{1-x}$ with FCC structure.

The mechanical properties of the synthesized high-entropy carbides are greatly dependent on their phase compositions and microstructures. The formation of a uniform solid solution of $(Ti_{0.2}Nb_{0.2}Ta_{0.2}Hf_{0.2}W_{0.2})C_x$ will enhance the hardness. The content of carbon vacancies will have a detrimental effect on the flexural strength. The fracture toughness of $(Ti_{0.2}Nb_{0.2}Ta_{0.2}Hf_{0.2}W_{0.2})C_x$ is regulated by the presence of the second phases and carbon vacancies. By optimization of the content of carbon vacancies, the particle size of raw powders, and sintering temperature, super mechanical properties (flexural strength is 743 MPa and fracture toughness is 8.6 MPa $m^{-1/2}$) were obtained in single-phase $(Ti_{0.2}Nb_{0.2}Ta_{0.2}Hf_{0.2}W_{0.2})C$ when sintered at 2000 °C from finer raw carbide powder.

## CRediT authorship contribution statement

**Wei Liao:** Writing – original draft, Methodology, Investigation, Data curation, Conceptualization. **Zhen Teng:** Writing – review & editing, Validation, Formal analysis. **Yiwang Bao:** Writing – review & editing, Validation, Resources.

## Declaration of competing interest

The authors declare that they have no known competing financial interests or personal relationships that could have appeared to influence the work reported in this paper.

## Acknowledgment

The work is supported by the Joint Fund of Henan Province Science and Technology R&D Program (Grant No. 225200810002)

## Appendix A. Supplementary data

Supplementary data to this article can be found online at https://doi.org/10.1016/j.ceramint.2024.10.429.

## References

[1] S. Yudin, S. Volodko, D. Moskovskikh, I. Alimov, A. Guryanov, S. Zhevnenko, H. Guo, A. Korotitsky, K. Sidnov, S. Roslyakov, C. Zhang, Fabrication of high-entropy carbide ceramics (Ti,Zr,Hf,Nb,Ta)C through low-temperature calcium-hydride reduction of oxides, J. Eur. Ceram. Soc. 43 (2023) 5108–5116, https://doi.org/10.1016/j.jeurceramsoc.2023.04.056.

[2] B. Ye, T. Wen, K. Huang, C.Z. Wang, Y. Chu, First-principles study, fabrication, and characterization of $(Hf_{0.2}Zr_{0.2}Ta_{0.2}Nb_{0.2}Ti_{0.2})C$ high-entropy ceramic, J. Am. Ceram. Soc. 102 (2019) 4344–4352, https://doi.org/10.1111/jace.16295.

[3] M.A. Tunes, S. Fritze, B. Osinger, P. Willenshofer, A.M. Alvarado, E. Martinez, A. S. Menon, P. Ström, G. Greaves, E. Lewin, U. Jansson, S. Pogatscher, T.A. Saleh, V. M. Vishnyakov, O. El-Atwani, From high-entropy alloys to high-entropy ceramics: the radiation-resistant highly concentrated refractory carbide (CrNbTaTiW)C, Acta Mater. 250 (2023), https://doi.org/10.1016/j.actamat.2023.118856.

[4] X.-F. Wei, J.-X. Liu, W. Bao, Y. Qin, F. Li, Y. Liang, F. Xu, G.-J. Zhang, High-entropy carbide ceramics with refined microstructure and enhanced thermal conductivity by the addition of graphite, J. Eur. Ceram. Soc. 41 (2021) 4747–4754, https://doi.org/10.1016/j.jeurceramsoc.2021.03.053.

[5] L. Feng, W.G. Fahrenholtz, G.E. Hilmas, Low-temperature sintering of single-phase, high-entropy carbide ceramics, J. Am. Ceram. Soc. 102 (2019) 7217–7224, https://doi.org/10.1111/jace.16672.

[6] J. Dusza, T. Csanádi, D. Medveď, R. Sedlák, M. Vojtko, M. Ivor, H. Ünsal, P. Tatarko, M. Tatarková, P. Šajgalík, Nanoindentation and tribology of a (Hf-Ta-Zr-Nb-Ti)C high-entropy carbide, J. Eur. Ceram. Soc. 41 (2021) 5417–5426, https://doi.org/10.1016/j.jeurceramsoc.2021.05.002.

[7] D. Liu, A. Zhang, J. Jia, J. Meng, B. Su, Phase evolution and properties of (VNbTaMoW)C high entropy carbide prepared by reaction synthesis, J. Eur. Ceram. Soc. 40 (2020) 2746–2751, https://doi.org/10.1016/j.jeurceramsoc.2020.03.020.

[8] T.J. Harrington, J. Gild, P. Sarker, C. Toher, C.M. Rost, O.F. Dippo, C. McElfresh, K. Kaufmann, E. Marin, L. Borowski, P.E. Hopkins, J. Luo, S. Curtarolo, D. W. Brenner, K.S. Vecchio, Phase stability and mechanical properties of novel high entropy transition metal carbides, Acta Mater. 166 (2019) 271–280, https://doi.org/10.1016/j.actamat.2018.12.054.

[9] Z. Huang, J. Zheng, M. Su, M. Deng, Y. Shi, R. Chen, Q. Wang, Z. Wang, J. Qi, R. Li, H. Wang, Rapid densification and mechanical properties of ultra-high-pressure sintered transition metal carbide ceramics, Ceram. Int. 49 (2023) 39850–39861, https://doi.org/10.1016/j.ceramint.2023.09.152.

[10] M.D. Hossain, T. Borman, A. Kumar, X. Chen, A. Khosravani, S.R. Kalidindi, E. A. Paisley, M. Esters, C. Oses, C. Toher, S. Curtarolo, J.M. LeBeau, D. Brenner, J. P. Maria, Carbon stoichiometry and mechanical properties of high entropy carbides, Acta Mater. 215 (2021), https://doi.org/10.1016/j.actamat.2021.117051.

[11] X. Zhang, N. Li, X. Chen, M. Stroup, Y. Lu, B. Cui, Direct selective laser sintering of high-entropy carbide ceramics, J. Mater. Res. 38 (2022) 187–197, https://doi.org/10.1557/s43578-022-00766-0.

[12] S.-C. Luo, W.-M. Guo, Z.-L. Fang, K. Plucknett, H.-T. Lin, Effect of carbon content on the microstructure and mechanical properties of high-entropy $(Ti_{0.2}Zr_{0.2}Nb_{0.2}Ta_{0.2}Mo_{0.2})C_x$ ceramics, J. Eur. Ceram. Soc. 42 (2022) 336–343, https://doi.org/10.1016/j.jeurceramsoc.2021.10.019.

[13] M.D. Hossain, T. Borman, C. Oses, M. Esters, C. Toher, L. Feng, A. Kumar, W. G. Fahrenholtz, S. Curtarolo, D. Brenner, J.M. LeBeau, J.P. Maria, Entropy landscaping of high-entropy carbides, Adv. Mater. 33 (2021) e2102904, https://doi.org/10.1002/adma.202102904.

[14] B. Ye, S. Ning, D. Liu, T. Wen, Y. Chu, One-step synthesis of coral-like high-entropy metal carbide powders, J. Am. Ceram. Soc. 102 (2019) 6372–6378, https://doi.org/10.1111/jace.16514.

[15] M. Tagir, R. Nikolay, P. Anatoliy, Synthesis of single-phase high-entropy carbides from a mixture of pre-mechanically alloyed CrNbMoWV HEA powders and carbon, Mater. Lett. 309 (2022), https://doi.org/10.1016/j.matlet.2021.131363.

[16] B. Li, C. Liu, Z. Fang, Z. Yang, F. Ding, L. Bai, C. Wang, F. Yuan, Synthesis of single-phase (ZrTiTaNbMo)C high-entropy carbide powders via magnesiothermic reduction process, J. Eur. Ceram. Soc. 42 (2022) 6767–6773, https://doi.org/10.1016/j.jeurceramsoc.2022.08.025.

[17] J. Zhang, B. Xu, Y. Xiong, S. Ma, Z. Wang, Z. Wu, S. Zhao, Design high-entropy carbide ceramics from machine learning, npj Comput. Mater. 8 (2022), https://doi.org/10.1038/s41524-021-00678-3.

[18] P. Sarker, T. Harrington, C. Toher, C. Oses, M. Samiee, J.P. Maria, D.W. Brenner, K. S. Vecchio, S. Curtarolo, High-entropy high-hardness metal carbides discovered by entropy descriptors, Nat. Commun. 9 (2018) 4980, https://doi.org/10.1038/s41467-018-07160-7.

[19] E. Chicardi, C. García-Garrido, F.J. Gotor, Low temperature synthesis of an equiatomic $(TiZrHfVNb)C_5$ high entropy carbide by a mechanically-induced carbon diffusion route, Ceram. Int. 45 (2019) 21858–21863, https://doi.org/10.1016/j.ceramint.2019.07.195.

[20] D. Liu, Y. Hou, A. Zhang, J. Han, J. Zhang, J. Meng, H. Su, Experimental studies on critical compositions for fabricating single-phase high entropy carbides based on the calculated phase diagram of $(VNbTaMoW)_{0.5}C_x$ ($0 < x < 0.6$), J. Eur. Ceram. Soc. 41 (2021) 7488–7497, https://doi.org/10.1016/j.jeurceramsoc.2021.08.037.

[21] D. Liu, Y. Hou, J. Meng, A. Zhang, J. Han, J. Zhang, The significant influence of carbon content on mechanical and thermal properties of $(VNbTaMoW)_{0.5}C_x$ high entropy carbides, J. Eur. Ceram. Soc. 42 (2022) 5262–5272, https://doi.org/10.1016/j.jeurceramsoc.2022.06.073.

[22] H. Chen, Z. Wu, M. Liu, W. Hai, W. Sun, Synthesis, microstructure and mechanical properties of high-entropy $(VNbTaMoW)C_5$ ceramics, J. Eur. Ceram. Soc. 41 (2021) 7498–7506, https://doi.org/10.1016/j.jeurceramsoc.2021.07.063.

[23] S. Kavak, K.G. Bayrak, M. Bellek, S. Mertdinç, F. Muhaffel, H. Gökçe, E. Ayas, B. Derin, M.L. Öveçoğlu, D. Ağaoğulları, Synthesis and characterization of (HfMoTiWZr)C high entropy carbide ceramics, Ceram. Int. 48 (2022) 7695–7705, https://doi.org/10.1016/j.ceramint.2021.11.317.

[24] X.-F. Wei, Y. Qin, J.-X. Liu, F. Li, Y.-C. Liang, G.-J. Zhang, Gradient microstructure development and grain growth inhibition in high-entropy carbide ceramics

prepared by reactive spark plasma sintering, J. Eur. Ceram. Soc. 40 (2020) 935–941, https://doi.org/10.1016/j.jeurceramsoc.2019.12.034.
[25] X.-F. Wei, J.-X. Liu, F. Li, Y. Qin, Y.-C. Liang, G.-J. Zhang, High entropy carbide ceramics from different starting materials, J. Eur. Ceram. Soc. 39 (2019) 2989–2994, https://doi.org/10.1016/j.jeurceramsoc.2019.04.006.
[26] J. Pötschke, M. Dahal, M. Herrmann, A. Vornberger, B. Matthey, A. Michaelis, Preparation of high-entropy carbides by different sintering techniques, J. Mater. Sci. 56 (2021) 11237–11247, https://doi.org/10.1007/s10853-021-06004-y.
[27] Y. Zhu, J. Chai, Z. Wang, T. Shen, L. Niu, S. Li, P. Jin, H. Zhang, J. Li, M. Cui, Microstructural damage evolution of (WTiVNbTa)$C_5$ high-entropy carbide ceramics induced by self-ions irradiation, J. Eur. Ceram. Soc. 42 (2022) 2567–2576, https://doi.org/10.1016/j.jeurceramsoc.2022.01.061.
[28] Y. Tan, W. Liao, Z. Teng, H. Zhang, Synthesis, mechanical, and thermophysical properties of high-entropy (Zr,Ti,Nb,Ta,Hf)$C_{0.8}$ ceramic, J. Am. Ceram. Soc. 106 (2023) 4382–4389, https://doi.org/10.1111/jace.19089.
[29] Y. He, C. Peng, S. Xin, K. Li, S. Liang, X. Lu, N. Kang, H. Xue, X. Shen, T. Shen, M. Wang, Vacancy effect on the preparation of high-entropy carbides, J. Mater. Sci. 55 (2020) 6754–6760, https://doi.org/10.1007/s10853-020-04471-3.
[30] J. Chen, Y. Zhu, J. Chai, L. Niu, T. Yan, B. Chen, T. Shen, H. Zang, Microstructure, mechanical, and thermal properties of (MoTaTiVW)CX high entropy ceramics with different carbon stoichiometries, Ceram. Int. 50 (2024) 28168–28176, https://doi.org/10.1016/j.ceramint.2024.05.116.
[31] J. Li, H. Fan, Q. Zhang, H. Chen, Y. Su, J. Song, L. Hu, Y. Zhang, Carbon vacancies enhanced oxidation resistance of high-entropy carbides ($Ti_{0.2}V_{0.2}Nb_{0.2}Mo_{0.2}W_{0.2}$)C, Ceram. Int. 50 (2023) 9926–9930, https://doi.org/10.1016/j.ceramint.2023.12.311.
[32] F. Wang, X. Zhang, X. Yan, Y. Lu, M. Nastasi, Y. Chen, B. Cui, The effect of submicron grain size on thermal stability and mechanical properties of high-entropy carbide ceramics, J. Am. Ceram. Soc. 103 (2020) 4463–4472, https://doi.org/10.1111/jace.17103.
[33] E. Chicardi, C. García-Garrido, J. Hernández-Saz, F.J. Gotor, Synthesis of all equiatomic five-transition metals High Entropy Carbides of the IVB (Ti, Zr, Hf) and VB (V, Nb, Ta) groups by a low temperature route, Ceram. Int. 46 (2020) 21421–21430, https://doi.org/10.1016/j.ceramint.2020.05.240.
[34] D. Liu, A. Zhang, J. Jia, J. Han, J. Zhang, J. Meng, A novel in-situ exothermic assisted sintering high entropy $Al_2O_3$/(NbTaMoW)C composites: microstructure and mechanical properties, Composites, Part B (2021) 212, https://doi.org/10.1016/j.compositesb.2021.108681.
[35] W. Zhang, K. Li, L. Chen, Z. Shi, S. Huo, B. Wei, S.-J.L. Kang, Y. Wang, Y. Zhou, The phase decomposition in non-equimolar (ZrHfVNbMoW)$C_x$ complex concentrated carbides via carbon content regulation, J. Eur. Ceram. Soc. 44 (2024) 1396–1403, https://doi.org/10.1016/j.jeurceramsoc.2023.10.050.
[36] M. Biesuz, T.G. Saunders, J. Veverka, M. Bortolotti, J. Vontorová, M. Vilémová, M. J. Reece, Solidification microstructures of multielement carbides in the high entropy Zr-Nb-Hf-Ta-$C_x$ system produced by arc melting, Scripta Mater. 203 (2021), https://doi.org/10.1016/j.scriptamat.2021.114091.
[37] G.V. Samsonov, M.S. Koval'chenko, R.Y. Petrykina, V.Y. Naumenko, Hot pressing of the transition metals and their carbides in their homogeneity regions, Sov. Powder Metall. Met. Ceram. 9 (1970) 713–716, https://doi.org/10.1007/bf00836960.
[38] E. Castle, T. Csanádi, S. Grasso, J. Dusza, M. Reece, Processing and properties of high-entropy ultra-high temperature carbides, Sci. Rep. 8 (2018), https://doi.org/10.1038/s41598-018-26827-1.
[39] P.A. Burr, S.X. Oliver, Formation and migration of point defects in tungsten carbide: unveiling the sluggish bulk self-diffusivity of WC, J. Eur. Ceram. Soc. 39 (2019) 165–172, https://doi.org/10.1016/j.jeurceramsoc.2018.10.001.
[40] J.X. Liu, L. Guo, Y. Wu, Y. Qin, Y. Liang, G.J. Zhang, Lattice rigidity in high-entropy carbide ceramics with carbon vacancies, J. Am. Ceram. Soc. 106 (2023) 5612–5619, https://doi.org/10.1111/jace.19206.
[41] X. Jin, C. Hou, Y. Zhao, Z. Wang, J. Wang, X. Fan, Mechanical properties and deformation mechanisms of ($Ti_{0.2}Zr_{0.2}Nb_{0.2}Hf_{0.2}Ta_{0.2}$)C high-entropy ceramics characterized by nanoindentation and scratch tests, Ceram. Int. 48 (2022) 35445–35451, https://doi.org/10.1016/j.ceramint.2022.08.147.
[42] Y. Wang, T. Csanádi, H. Zhang, J. Dusza, M.J. Reece, R.Z. Zhang, Enhanced hardness in high-entropy carbides through atomic randomness, Adv. Theor. Simul. 3 (2020), https://doi.org/10.1002/adts.202000111.
[43] Y. Tan, W. Liao, Z. Teng, X. Zhou, In situ reaction synthesis of high-entropy carbide/diboride composite with high mechanical properties, J. Am. Ceram. Soc. 107 (2023) 2565–2572, https://doi.org/10.1111/jace.19594.
[44] L. Chen, W. Zhang, Y. Tan, P. Jia, C. Xu, Y. Wang, X. Zhang, J. Han, Y. Zhou, Influence of vanadium content on the microstructural evolution and mechanical properties of (TiZrHfVNbTa)C high-entropy carbides processed by pressureless sintering, J. Eur. Ceram. Soc. 41 (2021) 60–67, https://doi.org/10.1016/j.jeurceramsoc.2021.09.011.
[45] Y. Fang, S. Zhao, C. Li, Y. Wu, J. Li, H. Fan, Mechanical and tribological performance of (TiNbTaWMo)C high-entropy ceramics in a wide temperature range, J. Mater. Res. Technol. 24 (2023) 6312–6321, https://doi.org/10.1016/j.jmrt.2023.04.220.
[46] W. Su, L. Chen, S. Huo, W. Zhang, Y. Wang, Y. Zhou, Fracture mode transition from intergranular to transgranular in (TiZrNbTaCr)C: the grain boundary purification effect of Cr carbide, J. Eur. Ceram. Soc. 44 (2024) 1881–1889, https://doi.org/10.1016/j.jeurceramsoc.2023.11.002.
[47] K. Lu, J.-X. Liu, X.-F. Wei, W. Bao, Y. Wu, F. Li, F. Xu, G.-J. Zhang, Microstructures and mechanical properties of high-entropy ($Ti_{0.2}Zr_{0.2}Hf_{0.2}Nb_{0.2}Ta_{0.2}$)C ceramics with the addition of SiC secondary phase, J. Eur. Ceram. Soc. 40 (2020) 1839–1847, https://doi.org/10.1016/j.jeurceramsoc.2019.12.056.
[48] D. Yu, J. Yin, B. Zhang, X. Liu, M.J. Reece, W. Liu, Z. Huang, Pressureless sintering and properties of ($Hf_{0.2}Zr_{0.2}Ta_{0.2}Nb_{0.2}Ti_{0.2}$)C high-entropy ceramics: the effect of pyrolytic carbon, J. Eur. Ceram. Soc. 41 (2021) 3823–3831, https://doi.org/10.1016/j.jeurceramsoc.2021.01.048.
[49] J. Song, G. Chen, H. Xiang, F. Dai, S. Dong, W. Han, X. Zhang, Y. Zhou, Regulating the formation ability and mechanical properties of high-entropy transition metal carbides by carbon stoichiometry, J. Mater. Sci. Technol. 121 (2022) 181–189, https://doi.org/10.1016/j.jmst.2021.12.063.
[50] L. Feng, W.T. Chen, W.G. Fahrenholtz, G.E. Hilmas, Strength of single-phase high-entropy carbide ceramics up to 2300°C, J. Am. Ceram. Soc. 104 (2020) 419–427, https://doi.org/10.1111/jace.17443.
[51] Y. Tan, Z. Teng, C. Chen, P. Jia, X. Zhou, H. Zhang, Compositional effect on mechanical properties of transition-metal carbide solid solutions, Ceram. Int. 47 (2021) 16882–16890, https://doi.org/10.1016/j.ceramint.2021.02.264.